Multiphoton above-threshold ionization in superintense free-electron x-ray laser fields: Beyond the dipole approximation

Zhongyuan Zhou[1,2,*] and Shih-I Chu[1,3,†]

[1]*Department of Chemistry, University of Kansas, Lawrence, Kansas 66045, USA*

[2]*Department of Physics and Astronomy, University of Georgia, Athens, Georgia 30602, USA*

[3]*Center for Quantum Science and Engineering, Department of Physics, National Taiwan University, Taipei 10617, Taiwan*

(Received 20 February 2011; revised manuscript received 19 December 2012; published 13 February 2013)

We present an accurate and efficient nondipole computational approach in momentum space for the nonperturbative study of multiphoton above-threshold ionization (ATI) of atoms in superintense and ultrashort-wavelength laser fields. This approach has been successfully used to investigate the multiphoton processes of a hydrogen atom exposed to superintense free-electron x-ray laser fields. We find that, compared to results of the dipole approximation, the nondipole ATI spectra are enhanced substantially in the high-energy regime, and the photoelectron angular distributions are distorted significantly in higher-intensity and/or longer-pulse laser fields; in particular two lobes are induced, one along and one against the laser propagation direction. The origin of these phenomena has been explored in detail.

DOI: 10.1103/PhysRevA.87.023407 PACS number(s): 32.80.Rm, 32.80.Fb, 33.80.Rv

I. INTRODUCTION

With the recent development of free-electron lasers (FELs), particularly the "fourth-generation" accelerator-based FELs [1–3], the study of multiphoton processes of atoms and molecules in superintense ultrashort-wavelength and x-ray laser fields is attracting more and more attention [4–9]. Theoretical investigation of the multiphoton processes in superintense and ultrashort-wavelength laser fields may encounter twofold difficulties. (1) In superintense laser fields, an electron can achieve extremely high energy and go to a place very far from the nucleus. To accurately calculate the wave function of the electron in spatial coordinate ($\mathcal{R}$) space, the boundary has to be set at a very large distance from the nucleus to avoid reflection. This requires the use of a very large number of grid points and thus makes the calculation difficult. (2) In superintense and ultrashort-wavelength laser fields, owing to the ionization of electrons the characteristic spatial scale of the system may be comparable to or even larger than the laser wavelength, and the spatial dependence of the laser fields may not be neglected. In this case, the dipole approximation is no longer a good approach; instead a nondipole approach that includes nondipole interactions is desirable. Due to the spatial dependence, a fully three-dimensional (3D) calculation is essential in the nondipole approach even for hydrogenlike atoms. Thus a huge number of grid points are necessary in the nondipole calculation, which is still a great challenge to currently available supercomputers.

To conquer the first difficulty, an efficient dipole computational approach has been proposed recently in momentum ($\mathcal{P}$) space [10]. This approach is based on the fact that the momentum of an electron is always finite and less than a certain maximum value k_M, and the probability of the electron is negligible when the electron momentum is greater than k_M. Thus the wave function of an electron can be calculated within a finite $\mathcal{P}$ space with a simple zero-boundary condition as long as the boundary is set at a properly large k_M. This approximation has been successfully used to study the multiphoton above-threshold ionization (ATI) spectra of a hydrogen atom in longer-wavelength and shorter-pulse laser fields where the nondipole interactions can be ignored.

To vanquish the second difficulty, an $\mathcal{R}$-space nondipole approach has been proposed within the Kramers-Henneberger frame by neglecting some higher-order nondipole interactions [11,12]. This approach has been used to study multiphoton ionization processes of a hydrogen atom interacting with XUV laser fields [11,12]. It is shown that the photoelectron angular distributions (PADs) are quite different from those of the dipole approximation when the pulse durations are larger than five optical cycles (OCs) for laser fields with field strength of 30 a.u. [12]. In particular, an extra lobe is induced against the laser propagation direction. However, the multiphoton ATI spectra are not obviously different from the dipole ones for laser pulses with a duration of *five* OCs [11]. This approach has also been used to investigate the multiphoton ionization processes of a hydrogen atom in excited states [13] and a hydrogen molecular ion H_2^+ [14]. The predicted PADs for these processes have multilobe structures.

In this paper, we propose a $\mathcal{P}$-space nondipole computational approach for the study of multiphoton ATI of atoms exposed to superintense ultrashort-wavelength laser fields. This approach includes all the nondipole interactions and has been applied to the calculation of multiphoton ATI spectra and PADs of a hydrogen atom in superintense x-ray (with wavelength $\lambda = 9.11$ nm) laser fields. It is shown that the ATI spectra are enhanced substantially in the high-energy region and the PADs are distorted significantly in higher-intensity and/or longer-pulse laser fields compared to those of the dipole approximation. In particular, two lobes are induced, one along and one against the laser propagation direction. The physical mechanism for these phenomena is explored.

II. THEORETICAL METHODOLOGY

A. Nondipole time-dependent Schrödinger equation

In the velocity gauge, the nondipole Hamiltonian of an electron in joint Coulomb and laser fields is given by

*zyzhou@uga.edu
†sichu@ku.edu

(atomic units are used throughout this paper unless otherwise indicated)

$$H(\mathbf{r},t) = \frac{1}{2}\left(\mathbf{p} + \frac{1}{c}\mathbf{A}\right)^2 + V(\mathbf{r}), \tag{1}$$

where $\mathbf{p} = -i\nabla$ is the electron momentum operator, $V(\mathbf{r})$ is the Coulomb potential, c is the speed of light in vacuum, and $\mathbf{A}(\mathbf{r},t)$ is the vector potential of the laser field. For a sine-squared laser pulse linearly polarized along the x axis and propagated along the z axis, the vector potential is

$$\mathbf{A}(\mathbf{r},t) = \mathbf{e}_x \frac{cE_0}{\omega} \sin^2\left(\frac{\pi\eta}{\omega T_P}\right)\sin(\eta+\phi), \tag{2}$$

where E_0 is the laser field strength, T_P is the pulse duration, ϕ is the carrier-envelope phase, $\eta = \omega t - \mathbf{k}_L\cdot\mathbf{r}$, $\mathbf{k}_L = k_L\mathbf{e}_z$, $k_L = 2\pi/\lambda = \omega/c$, ω is the laser angular frequency, $\mathbf{e}_x$ is the unit vector along the x axis, and $\mathbf{e}_z$ is the unit vector along the z axis. For the laser fields considered here, the propagation direction is perpendicular to the polarization direction and thus $\mathbf{k}_L \perp \mathbf{A}$. In the Coulomb gauge, $\nabla\cdot\mathbf{A} = 0$ and the nondipole Hamiltonian Eq. (1) is recast to

$$H(\mathbf{r},t) = \frac{1}{2}\left(\mathbf{p}^2 + \frac{2}{c}\mathbf{A}\cdot\mathbf{p} + \frac{\mathbf{A}^2}{c^2}\right) + V(\mathbf{r}). \tag{3}$$

The $\mathcal{R}$-space nondipole time-dependent Schrödinger equation (TDSE) is

$$i\frac{\partial}{\partial t}\Phi(\mathbf{r},t) = H(\mathbf{r},t)\,\Phi(\mathbf{r},t). \tag{4}$$

The relation between the $\mathcal{R}$-space wave function $\Phi(\mathbf{r},t)$ and the $\mathcal{P}$-space wave function $\varphi(\mathbf{k},t)$ is given by the Fourier transform

$$\Phi(\mathbf{r},t) = \frac{1}{(2\pi)^{3/2}}\int \varphi(\mathbf{k},t)\exp(i\mathbf{k}\cdot\mathbf{r})\,d\mathbf{k}. \tag{5}$$

Applying Eqs. (3) and (5) to Eq. (4), multiplying Eq. (4) by $\exp(-i\mathbf{k}\cdot\mathbf{r})$, and integrating Eq. (4) over $\mathbf{r}$, we obtain the $\mathcal{P}$-space nondipole TDSE

$$i\frac{\partial\varphi(\mathbf{k},t)}{\partial t} = \int H(\mathbf{k},\mathbf{k}',t)\,\varphi(\mathbf{k}',t)d\mathbf{k}', \tag{6}$$

with the $\mathcal{P}$-space Hamiltonian given by

$$H(\mathbf{k},\mathbf{k}',t) = \frac{\mathbf{k}^2}{2}\delta(\mathbf{k}-\mathbf{k}') + V(\mathbf{k},\mathbf{k}') + D(\mathbf{k},\mathbf{k}',t) + B(\mathbf{k},\mathbf{k}',t), \tag{7}$$

where

$$V(\mathbf{k},\mathbf{k}') = \frac{1}{(2\pi)^3}\int V(\mathbf{r})\exp[i(\mathbf{k}'-\mathbf{k})\cdot\mathbf{r}]d\mathbf{r}, \tag{8}$$

$$D(\mathbf{k},\mathbf{k}',t) = \frac{1}{(2\pi)^3}\int\left[\frac{1}{2c}\mathbf{A}\cdot(\mathbf{k}+\mathbf{k}')\right]\exp[i(\mathbf{k}'-\mathbf{k})\cdot\mathbf{r}]d\mathbf{r}, \tag{9}$$

and

$$B(\mathbf{k},\mathbf{k}',t) = \frac{1}{(2\pi)^3}\int\left(\frac{\mathbf{A}^2}{2c^2}\right)\exp[i(\mathbf{k}'-\mathbf{k})\cdot\mathbf{r}]d\mathbf{r}, \tag{10}$$

are the $\mathcal{P}$-space Coulomb potential and laser-electron interactions, respectively. In general, the $\mathcal{P}$-space Coulomb potential is calculated from the $\mathcal{R}$-space Coulomb potential via the Fourier transform Eq. (8). For a hydrogenlike atom, the $\mathcal{P}$-space Coulomb potential can be calculated analytically. For a hydrogenlike atom with a nuclear charge Z, the $\mathcal{P}$-space Coulomb potential is given by

$$V(\mathbf{k},\mathbf{k}') = \frac{1}{(2\pi)^3}\int\left(-\frac{Z}{|\mathbf{r}|}\right)\exp[i(\mathbf{k}'-\mathbf{k})\cdot\mathbf{r}]d\mathbf{r} = -\frac{Z}{2\pi^2}\frac{1}{|\mathbf{k}-\mathbf{k}'|^2}. \tag{11}$$

This potential has a quadratic singularity at $\mathbf{k} = \mathbf{k}'$ [15,16]. For an arbitrary one-electron binding potential, the $\mathcal{P}$-space counterpart can be computed numerically. Since the binding potential decreases with the radial distance of electron from nucleus the integral in the Fourier transform is integrable and the $\mathcal{P}$-space potential can be numerically computed. Because the binding potential is time independent the $\mathcal{P}$-space binding potential is also time independent and needs to be calculated only once on the $\mathcal{P}$-space grid points before the $\mathcal{P}$-space wave-function propagation. For the vector potential given by Eq. (2), $D(\mathbf{k},\mathbf{k}',t)$ and $B(\mathbf{k},\mathbf{k}',t)$ are calculated by Eqs. (A1) and (A2) in Appendix A, respectively.

B. Partial-wave expansion and radial wave function

To calculate the wave function, the $\mathcal{P}$-space Coulomb potential $V(\mathbf{k},\mathbf{k}')$ is expanded, in spherical coordinates, in partial waves as

$$V(\mathbf{k},\mathbf{k}') = \frac{1}{kk'}\sum_{lml'm'} V_l(k,k')Y_{lm}(\theta,\phi)Y^*_{l'm'}(\theta',\phi')\delta_{ll'}\delta_{mm'}, \tag{12}$$

where $k = |\mathbf{k}|$, $Y_{lm}(\theta,\phi)$ is the spherical harmonic, and $V_l(k,k')$ is the partial-wave Coulomb potential given by

$$V_l(k,k') = kk'\sum_{l'm'}\int\int Y^*_{lm}(\theta,\phi)V(\mathbf{k},\mathbf{k}')Y_{l'm'}(\theta',\phi')d\Omega\,d\Omega'. \tag{13}$$

Here, $d\Omega = \sin\theta\,d\theta\,d\phi$, $l\in[0,L_M]$, $m\in[-l,l]$, and L_M is the maximum number of partial waves. For hydrogenlike atoms, the partial-wave Coulomb potential is calculated by

$$V_l(k,k') = -\frac{Z}{\pi}Q_l(z), \tag{14}$$

where $z = (k^2+k'^2)/2kk'$ and $Q_l(z)$ is the Legendre function of the second kind [15,16]. It has a logarithmic singularity at $k = k'$.

Similarly, the $\mathcal{P}$-space laser-electron interaction terms $D(\mathbf{k},\mathbf{k}',t)$ and $B(\mathbf{k},\mathbf{k}',t)$ can be expanded in partial waves as

$$D(\mathbf{k},\mathbf{k}',t) = \frac{1}{kk'}\sum_{lml'm'} D_{lm,l'm'}(k,k',t)Y_{lm}(\theta,\phi)Y^*_{l'm'}(\theta',\phi') \tag{15}$$

and

$$B(\mathbf{k},\mathbf{k}',t)=\frac{1}{kk'}\sum_{lml'm'}B_{lm,l'm'}(k,k',t)Y_{lm}(\theta,\phi)Y^{*}_{l'm'}(\theta',\phi'), \tag{16}$$

where the partial-wave laser-electron interaction terms $D_{lm,l'm'}(k,k',t)$ and $B_{lm,l'm'}(k,k',t)$ can be calculated by

$$D_{lm,l'm'}(k,k',t)=kk'\int\!\!\int Y^{*}_{lm}(\theta,\phi)D(\mathbf{k},\mathbf{k}',t)Y_{l'm'}(\theta',\phi')d\Omega\,d\Omega' \tag{17}$$

and

$$B_{lm,l'm'}(k,k',t)=kk'\int\!\!\int Y^{*}_{lm}(\theta,\phi)B(\mathbf{k},\mathbf{k}',t)Y_{l'm'}(\theta',\phi')d\Omega\,d\Omega', \tag{18}$$

respectively. For the laser pulse given by Eq. (2), $D_{lm,l'm'}(k,k',t)$ and $B_{lm,l'm'}(k,k',t)$ are calculated using Eqs. (B1) and (B2) in Appendix B, respectively.

The wave function $\varphi(\mathbf{k},t)$ is expanded in partial waves as

$$\varphi(\mathbf{k},t)=\frac{1}{k}\sum_{lm}R_{lm}(k,t)Y_{lm}(\theta,\phi), \tag{19}$$

where $R_{lm}(k,t)$ is the $\mathcal{P}$-space radial wave function.

Substituting Eqs. (7), (12), (15), (16), and (19) into Eq. (6), multiplying Eq. (6) by $Y_{lm}(\theta,\phi)$, and integrating Eq. (6) over the angles (θ,ϕ), we obtain an integro-differential equation for the $\mathcal{P}$-space radial wave function $R_{lm}(k,t)$:

$$\begin{aligned}i\frac{\partial R_{lm}(k,t)}{\partial t}=&\frac{k^2}{2}R_{lm}(k,t)+\int V_l(k,k')R_{lm}(k',t)dk'\\&+\sum_{l'm'}\int D_{lm,l'm'}(k,k',t)R_{l'm'}(k',t)dk'\\&+\sum_{l'm'}\int B_{lm,l'm'}(k,k',t)R_{l'm'}(k',t)dk'.\end{aligned} \tag{20}$$

For longer-wavelength, lower-intensity, and shorter-pulse laser fields, $\mathbf{k}_L\cdot\mathbf{r}\sim r/\lambda\to 0$ and the dependence of $\mathbf{A}$ on spatial coordinates can be neglected. In this case, $D(\mathbf{k},\mathbf{k}',t)=\mathbf{A}\cdot\mathbf{k}\delta(\mathbf{k}'-\mathbf{k})/c$ and $B(\mathbf{k},\mathbf{k}',t)=\mathbf{A}^2\delta(\mathbf{k}'-\mathbf{k})/2c^2$. After substituting Eq. (7) into Eq. (6), the third term on the right-hand side (RHS) of Eq. (6), $(\mathbf{A}\cdot\mathbf{k}/c)\varphi(\mathbf{k},t)$, represents the dipole interaction while the fourth term, $(\mathbf{A}^2/2c^2)\varphi(\mathbf{k},t)$, only changes the phase of the wave function and thus can be removed using a transform. In this case, Eq. (6) is degraded to the equation of the dipole approximation [10].

III. NUMERICAL RECIPES

A. Landé subtraction technique

To remove the singularity in the Coulomb potential, the Landé subtraction technique [15,17] is applied to the calculation of the term containing $V_l(k,k')$. Based on this technique, the second term on the RHS of Eq. (20) can be computed from [10]

$$\begin{aligned}&\int V_l(k,k')R_{lm}(k',t)dk'\\&=kS_lR_{lm}(k,t)+\int V_l(k,k')\left[R_{lm}(k',t)-\frac{R_{lm}(k,t)}{P_l(z)}\frac{k}{k'}\right]dk',\end{aligned} \tag{21}$$

where $P_l(z)$ is the Legendre polynomial, and S_l is given by

$$S_l=\int\frac{V_l(k,k')}{P_l(z)}\frac{dk'}{k'}, \tag{22}$$

and can be calculated numerically [18]. Introducing the singularity-free potential

$$v_l(k,k')=\begin{cases}0, & k'=k,\\ V_l(k,k'), & k'\neq k,\end{cases} \tag{23}$$

substituting Eq. (21) into Eq. (20), and using Eq. (23), we achieve a singularity-free equation for the $\mathcal{P}$-space radial wave function $R_{lm}(k,t)$,

$$\begin{aligned}i\frac{\partial R_{lm}(k,t)}{\partial t}=&\left[\frac{k^2}{2}+kS_l-kq_l(k)\right]R_{lm}(k,t)\\&+\sum_{l'm'}\int v_l(k,k')\delta_{ll'}\delta_{mm'}R_{l'm'}(k',t)dk'\\&+\sum_{l'm'}\int D_{lm,l'm'}(k,k',t)R_{l'm'}(k',t)dk'\\&+\sum_{l'm'}\int B_{lm,l'm'}(k,k',t)R_{l'm'}(k',t)dk',\end{aligned} \tag{24}$$

where

$$q_l(k)=\int\frac{v_l(k,k')}{P_l(z)}\frac{dk'}{k'}. \tag{25}$$

By solving Eq. (24) the $\mathcal{P}$-space radial wave function is obtained, from which the ATI spectra and PADs are calculated.

B. $\mathcal{P}$-space generalized pseudospectral method

To solve Eq. (24), we extend the $\mathcal{R}$-space generalized pseudospectral (GPS) method [19,20] to the $\mathcal{P}$ space [10]. Since the $\mathcal{P}$-space wave function can be set to zero on the boundary with the momentum k_M, we will confine our calculations to the volume of $k\in[0,k_M]$. To use the GPS method, the $\mathcal{P}$-space domain $k\in[0,k_M]$ is mapped to a new domain $x\in[-1,1]$ by the mapping function

$$k(x)=\gamma\frac{1+x}{1-x+x_M}, \tag{26}$$

where $x_M=2\gamma/k_M$ and γ is a mapping parameter. The smaller the value of γ, the denser the grid points at small momentum k. By using the mapping function, the grid points can be adjusted flexibly in some range and the calculation is improved. It has been shown that for $\mathcal{R}$-space calculations involving Coulomb potentials [19,20], the eigenvalues and eigenfunctions achieved by using the mapped grid points are more accurate than those of equal-spacing grid points if the same number of grid points are used in the computation. It has also been shown that the GPS method with the mapping

function (26) is a very accurate method for the $\mathcal{P}$-space calculation [10].

To calculate the radial wave function, Eq. (24) is mapped to the domain $x \in [-1,1]$ and discretized by using Gaussian quadrature with N_M grid points. Then a time-dependent (TD) matrix equation is obtained:

$$i\frac{dy_{jlm}(t)}{dt} = \left[\frac{k_j^2}{2} + k_j S_l - k_j q_{jl}\right] y_{jlm}(t) + \sum_{j'=1}^{N} u^l_{jj'} y_{j'lm}(t) + \sum_{j'l'm'} f_{jlm,j'l'm'} y_{j'l'm'}(t), \tag{27}$$

with

$$y_{jlm}(t) = \sqrt{\dot{k}_j w_j} R_{jlm}(t), \tag{28}$$

$$u^l_{jj'} = v^l_{jj'}\sqrt{\dot{k}_j w_j \dot{k}_{j'} w_{j'}}, \tag{29}$$

and

$$f_{jlm,j'l'm'} = (D_{jlm,j'l'm'} + B_{jlm,j'l'm'})\sqrt{\dot{k}_j w_j \dot{k}_{j'} w_{j'}}, \tag{30}$$

where w_j is the weight of the Gaussian quadrature, the subscript j denotes the jth grid point, $k_j = k(x_j)$, $R_{jlm} = R_{lm}(k_j,t)$, $\dot{k}_j = dk/dx|_{x_j}$, $q_{jl} = q_l(k_j)$, $v^l_{jj'} = v_l(k_j,k_{j'})$, $B_{jlm,j'l'm'} = B_{lm,l'm'}(k_j,k_{j'},t)$, and $D_{jlm,j'l'm'} = D_{lm,l'm'}(k_j,k_{j'},t)$. From Eqs. (B1) to (B4), $D_{lm,l'm'}(k,k',t) \neq 0$ when and only when $m' = m \pm 1$ and $B_{lm,l'm'}(k,k',t) \neq 0$ when and only when $m' = m$. Thus the matrix element $f_{jlm,j'l'm'} \neq 0$ when and only when $m' = m$ or $m \pm 1$ and the matrix $\mathbf{F} = \{f_{jlm,j'l'm'}\}$ is sparse.

For convenience, Eq. (27) is rewritten in matrix form as

$$i\frac{d}{dt}\mathbf{Y}(t) = [\mathbf{H}_0 + \mathbf{F}(t)]\,\mathbf{Y}(t), \tag{31}$$

where $\mathbf{Y}(t) = \{y_{jlm}(t)\}$, $\mathbf{H}_0 = \{h^l_{jj'}\delta_{ll'}\delta_{mm'}\}$, and $\mathbf{F}(t) = \{f_{jlm,j'l'm'}\}$. Here, $h^l_{jj'}$ is the unperturbed Hamiltonian matrix element given by

$$h^l_{jj'} = \left(\frac{k_j^2}{2} + k_j S_l - k_j q_{jl}\right)\delta_{jj'} + u^l_{jj'}. \tag{32}$$

C. Propagation of the wave function

Solution of the TD matrix equation (31) is a demanding task due to the very large dimension of the matrix equation for superintense laser fields. However, since the matrix $\mathbf{F}(t)$ is sparse, the Hamiltonian matrix $\mathbf{H}_0 + \mathbf{F}(t)$ is also sparse. To fully take advantage of the property of the sparse matrix, we employ the symplectic algorithm [21] to propagate the TD matrix equation (31). The symplectic algorithm keeps the norm of the wave function reserved and allows large time steps in the propagation of the wave function. One of the frequently used symplectic algorithms is the Euler midpoint algorithm. Applying this algorithm to Eq. (31), one has

$$\frac{\mathbf{Y}^{n+1} - \mathbf{Y}^n}{\Delta t} = -i[\mathbf{H}_0 + \mathbf{F}^{n+1/2}]\mathbf{Y}^{n+1/2}, \tag{33}$$

where the superscript $n+1/2$ represents the value at the midpoint time $t_n + \Delta t/2$. Making use of the approximation

$$\mathbf{Y}^{n+1/2} \approx \frac{\mathbf{Y}^{n+1} + \mathbf{Y}^n}{2}, \tag{34}$$

Eq. (33) can be written as

$$(1 - \mathbf{Q}^{n+1/2})\mathbf{Y}^{n+1} = (1 + \mathbf{Q}^{n+1/2})\mathbf{Y}^n, \tag{35}$$

with

$$\mathbf{Q}^{n+1/2} = -\frac{i\Delta t}{2}[\mathbf{H}_0 + \mathbf{F}^{n+1/2}]. \tag{36}$$

Since the coefficient matrix is sparse the algebraic equation (35) can be solved by using high-performance and memory-efficient software packages. One of such packages is PARDISO, a package of parallel sparse, direct, and multirecursive interactive linear solvers [22], which will be used in our calculations.

IV. ABOVE-THRESHOLD IONIZATION AND PHOTOELECTRON ANGULAR DISTRIBUTION

To isolate the continuum-state wave function from the total wave function so as to calculate the ionization probability and photoelectron distribution, we introduce a bound-state projection operator $\widehat{P}_B$ and a continuum-state projection operator $\widehat{P}_C$, respectively, by

$$\widehat{P}_B = \sum_{\text{all } E_\alpha<0} |\psi_\alpha\rangle\langle\psi_\alpha| \tag{37}$$

and

$$\widehat{P}_C = \sum_{\text{all } E_\alpha\geqslant 0} |\psi_\alpha\rangle\langle\psi_\alpha|, \tag{38}$$

where E_α and $|\psi_\alpha(\mathbf{k})\rangle$ are the eigenvalue and eigenfunction of the unperturbed Hamiltonian $\mathbf{H}_0$. Obviously $\widehat{P}_B + \widehat{P}_C = I$. Using the projection operators, the bound-state wave function $\varphi_B(\mathbf{k},t)$ and continuum-state wave function $\varphi_C(\mathbf{k},t)$ can be calculated from the total wave function $\varphi(\mathbf{k},t)$ by

$$\varphi_B(\mathbf{k},t) = \widehat{P}_B\varphi(\mathbf{k},t) = \sum_{\text{all } E_\alpha<0} c_\alpha |\psi_\alpha(\mathbf{k})\rangle \tag{39}$$

and

$$\varphi_C(\mathbf{k},t) = \widehat{P}_C\varphi(\mathbf{k},t) = \sum_{\text{all } E_\alpha\geqslant 0} c_\alpha |\psi_\alpha(\mathbf{k})\rangle, \tag{40}$$

respectively. Here, $c_\alpha = \langle\psi_\alpha(\mathbf{k})|\varphi(\mathbf{k},t)\rangle$ is the coefficient and $|c_\alpha|^2$ is the probability on the unperturbed eigenstate α.

The multiphoton ATI spectra and PADs can be calculated directly from the $\mathcal{P}$-space wave function [10]. At the end of the laser pulse ($t = t_f$), the triple-differential ionization probability density of a photoelectron having momentum $\mathbf{k} = (k,\theta,\phi)$ is given by

$$\frac{dP(\mathbf{k})}{d\mathbf{k}} = \frac{\partial^3 P}{k^2\partial k\partial\Omega} = |\varphi_C(\mathbf{k},t_f)|^2, \tag{41}$$

where $d\mathbf{k} = k^2 dk\, d\Omega$. The triple-differential ionization probability density of a photoelectron having kinetic energy $E = k^2/2$ and along the direction $\widehat{\mathbf{k}} = (\theta,\phi)$ is computed from

$$\frac{\partial^3 P}{\partial E\partial\Omega} = k\frac{dP(\mathbf{k})}{d\mathbf{k}} = k|\varphi_C(\mathbf{k},t_f)|^2. \tag{42}$$

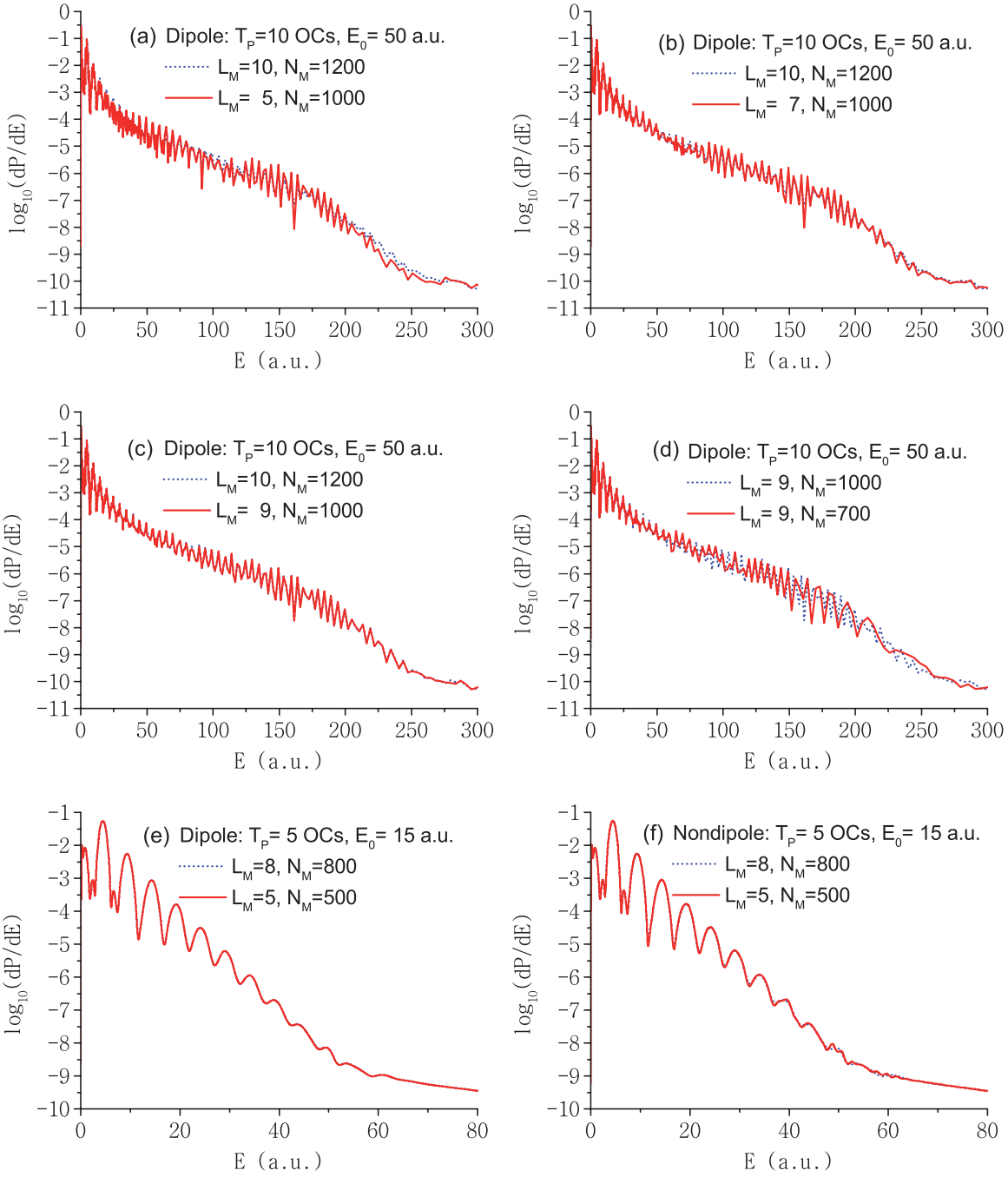

FIG. 1. (Color online) ATI spectra for different L_M and N_M: (a)–(d) the dipole ATI spectra for $E_0 = 50$ a.u. and $T_P = 10$ OCs, (e) the dipole, and (f) the nondipole ATI spectra for $E_0 = 15$ a.u. and $T_P = 5$ OCs.

The double-differential ionization probability that describes the PADs is

$$\frac{\partial^2 P}{\partial \Omega} = \int |\varphi_C(\mathbf{k},t_f)|^2 k^2 dk, \tag{43}$$

the differential ionization probability that characterizes the ATI spectra is given by

$$\frac{dP}{dE} = \int k|\varphi_C(\mathbf{k},t_f)|^2 d\Omega, \tag{44}$$

and the total ionization probability is

$$P = \int |\varphi_C(\mathbf{k},t_f)|^2 d\mathbf{k}. \tag{45}$$

V. RESULTS AND DISCUSSION

The proposed approach has been applied to the study of multiphoton ATI of a hydrogen atom in superintense x-ray laser fields with $\omega = 5.0$ a.u. ($\lambda = 9.11$ nm) and $\phi = 0$. The maximum number of partial waves L_M and grid points N_M

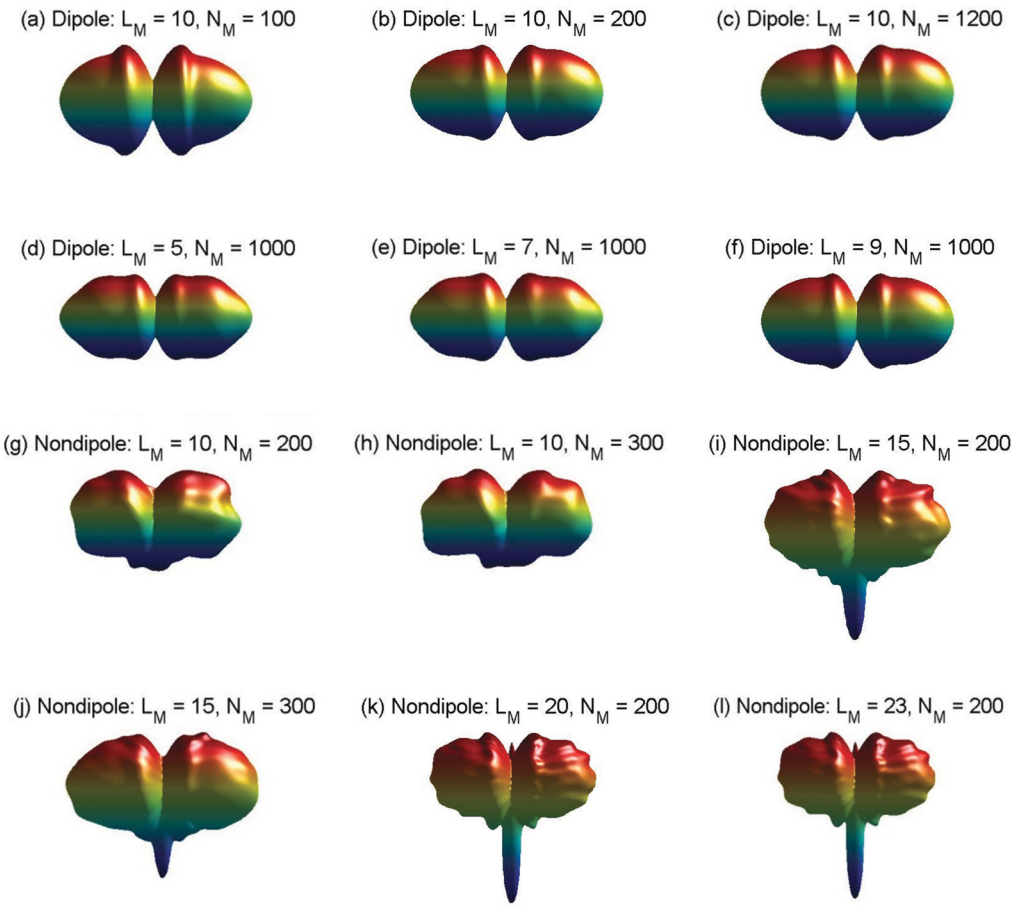

FIG. 2. (Color online) PADs for different L_M and N_M: (a)–(f) the dipole and (g)–(l) the nondipole PADs for $E_0 = 50$ a.u. and $T_P = 10$ OCs.

used in the calculation vary with the field strength and pulse duration. More partial waves and grid points are needed for higher-intensity and/or longer-pulse laser fields. In general, converged ATI spectra and PADs are acquired when enough large values of L_M and N_M are employed. However, for the laser intensities and pulse durations considered here, particularly for $E_0 = 50$ a.u. and $T_P = 10$ OCs, the 3D nondipole calculations are still challenges to midsize supercomputers when the same L_M and N_M are used in the computation of both ATI spectra and PADs. Fortunately, we find that converged ATI spectra and PADs can be obtained by using different values of L_M and N_M.

To find suitable values of the pair (L_M, N_M) for converged calculations of ATI spectra and PADs, we have performed comprehensive computations using different values of (L_M, N_M). In Figs. 1(a) to 1(d), the dipole ATI spectra are plotted for $E_0 = 50$ a.u. and $T_P = 10$ OCs. It is shown that the ATI spectra do not change much with L_M when $L_M \geqslant 7$ for $N_M \geqslant 1000$ [see Figs. 1(a)–1(c)] but vary greatly with N_M even for $L_M = 9$ [see Fig. 1(d)] when $N_M < 1000$. Thus the ATI spectra are more sensitive to N_M when N_M is less than some value, and converged ATI spectra can be obtained by using smaller L_M as long as N_M is large enough. In Figs. 1(e) and 1(f), the dipole and nondipole ATI spectra are displayed, respectively, for $E_0 = 15$ a.u. and $T_P = 5$ OCs using different values of (L_M, N_M). It is shown that converged nondipole ATI spectra can be achieved when the same values of (L_M, N_M) are employed as for the converged dipole calculations. Thus in the calculations of ATI spectra the values of $(L_M, N_M) = (5,400)$ for $E_0 = 10$ a.u. and $T_P = 3$ OCs to $(L_M, N_M) = (7,1000)$ for $E_0 = 50$ a.u. and $T_P = 10$ OCs are employed.

In Fig. 2 the PADs obtained from the calculations using different values of (L_M, N_M) are plotted for $E_0 = 50$ a.u. and $T_P = 10$ OCs. Figures 2(a)–2(c) show that the dipole PAD obtained from the calculation with $(L_M, N_M) = (10,200)$ is very close to that with $(L_M, N_M) = (10,1200)$ and the PADs are insensitive to N_M when $N_M \geqslant 200$ for $L_M = 10$. Figures 2(d)–2(f) show that the PAD with $(L_M, N_M) = (5,1000)$ is quite different from that with $(L_M, N_M) = (9,1000)$ and thus the PADs are more sensitive to L_M than to N_M. In Figs. 2(g)–2(l) the nondipole PADs are displayed. It is shown that the nondipole PADs are also insensitive to N_M but quite sensitive to L_M. From Figs. 2(g) and 2(h) as well as Figs. 2(i) and 2(j), we see that for the same L_M the PAD using $N_M = 200$ is very close to that using $N_M = 300$. Thus the PAD using $N_M = 200$ is converged. From Figs. 2(k) and 2(l), the PADs using $(L_M, N_M) = (20,200)$ and $(L_M, N_M) = (23,200)$ are very close to each other. Thus we employ $(L_M, N_M) = (20,200)$ in the calculations of PADs.

Using the parameters above, the ATI spectra and PADs of a hydrogen atom in superintense x-ray laser fields are computed using the nondipole $\mathcal{P}$-space approach for the

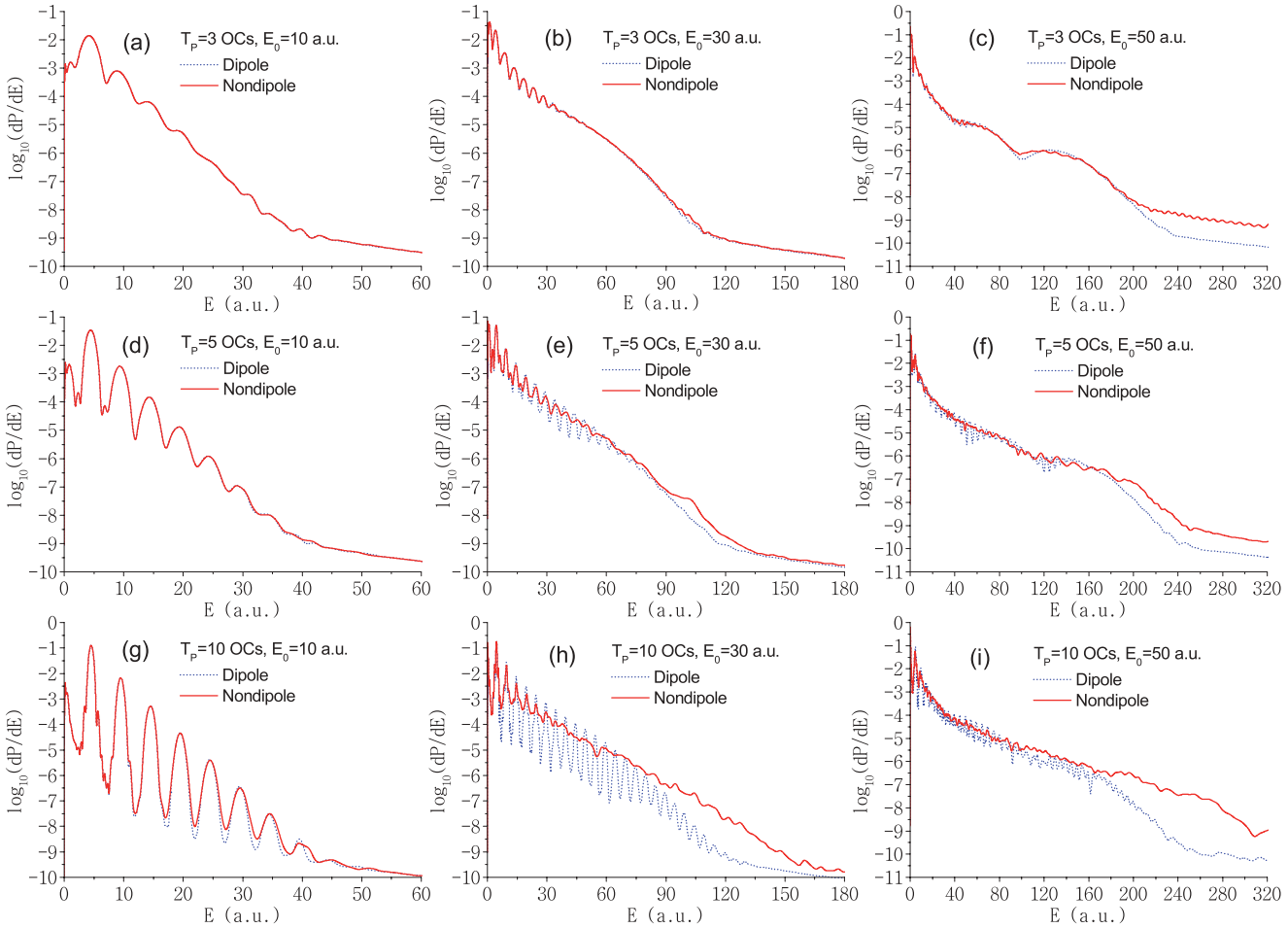

FIG. 3. (Color online) Dipole (blue dashed curves) and nondipole (red solid curves) ATI spectra of a hydrogen atom in x-ray laser fields with different laser intensities and pulse durations.

laser field strengths $E_0 = 10$, 30, and 50 a.u. and the laser pulse durations $T_P = 3$, 5, and 10 OCs. In Fig. 3, the nondipole ATI spectra are plotted together with those from the dipole approximation [10] for comparison. It is shown that in the shorter-pulse and lower-intensity laser fields the nondipole ATI spectra are almost identical with the dipole ones, as displayed in Figs. 3(a), 3(b), and 3(d). With increase of the laser intensity and/or pulse duration, the ATI spectra from the two approaches become gradually separated from each other. In longer-pulse and/or higher-intensity laser fields, the nondipole ATI spectra are quite different from the dipole ones, as shown in Figs. 3(h) and 3(i). Compared to the dipole ATI spectra, the relative peak heights (the difference between the maxima and minima) of the nondipole ATI spectra are much smaller and thus the ATI peaks become less well resolved on the scales of the figures. Moreover, the nondipole ATI spectra are enhanced substantially in the high-energy region, demonstrating the underestimation of the dipole approximation to the ionization probability of high-energy electrons.

To explore the mechanism of the enhancement of the ATI spectra in the high-energy region, we study dipole and nondipole laser-electron interactions. From Eq. (2), the spatial dependence of the laser field $\mathbf{A}(\mathbf{r},t)$ comes from two terms that contain $\mathbf{k}_L \cdot \mathbf{r}$ in the envelope factor $\sin^2(\pi\eta/\omega T_P)$ and the oscillation term $\sin(\eta+\phi)$. They are given by $f_1 = (\pi/\omega T_P)(\mathbf{k}_L \cdot \mathbf{r})$ and $f_2 = \mathbf{k}_L \cdot \mathbf{r}$, respectively. For a laser field with pulse duration of $N_{\rm OC}$ OCs the ratio $f_1/f_2 = \pi/\omega T_P = 1/2N_{\rm OC}$ is negligibly small when $N_{\rm OC} \geqslant 3$. In this case, the spatial dependence in the envelope factor can fairly be neglected compared to that in the oscillation term. Using the Taylor series of the sine function, $\mathbf{A}(\mathbf{r},t)$ can be well approximated by

$$\mathbf{A}(\mathbf{r},t) \approx \mathbf{e}_x \frac{cE_0}{\omega} \sin^2\left(\frac{\pi t}{T_P}\right) \sum_{n=0}^{\infty} a_n (\mathbf{k}_L \cdot \mathbf{r})^n , \qquad (46)$$

where $a_n = (-1)^n g_n(\omega t+\phi)/n!$ and $g_n(x) = d^n \sin x/dx^n$. On the RHS of Eq. (46), the first term with $n = 0$ is the dipole term, and all the others proportional to $(\mathbf{k}_L \cdot \mathbf{r})^n$ with $n > 0$ are nondipole terms. The dipole term is inversely proportional to ω (proportional to λ) and independent of $\mathbf{k}_L \cdot \mathbf{r}$, while the nondipole interaction terms are proportional to $\mathbf{k}_L \cdot \mathbf{r}$ and ω (inversely proportional to λ) except for the term with $n = 1$ which is independent of ω (and λ). In shorter-wavelength (higher-frequency) and/or higher-intensity and/or longer-pulse laser fields, the nondipole interaction terms $(\mathbf{k}_L \cdot \mathbf{r})^n$ may not be much smaller than the dipole interaction term, particularly for processes involving ionization where the photoelectron

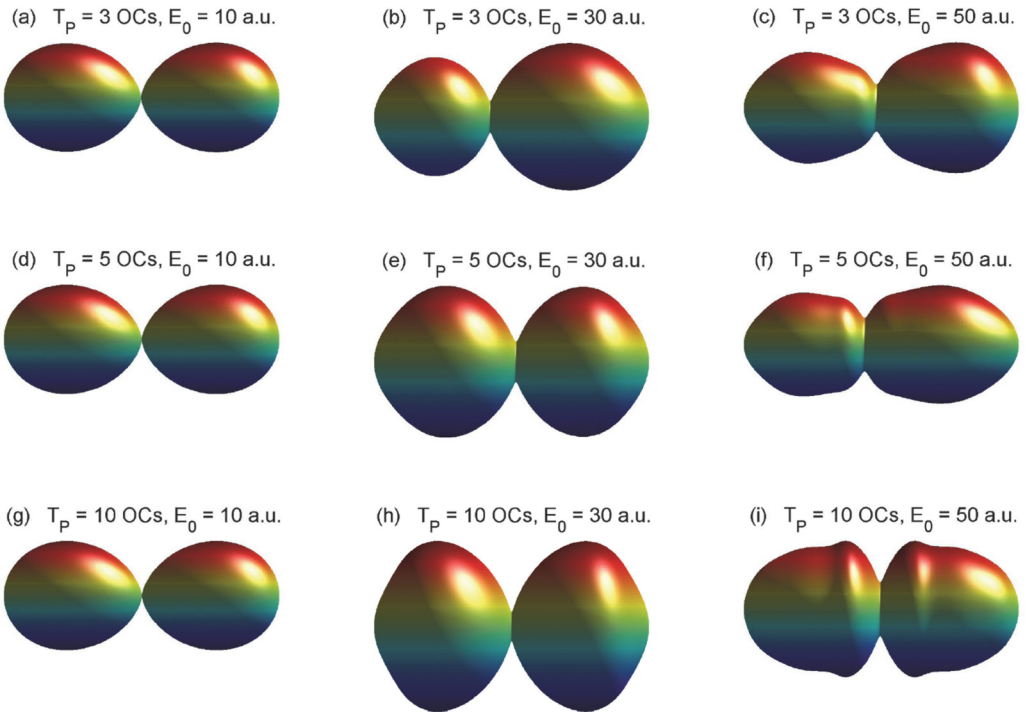

FIG. 4. (Color online) Dipole PADs in x-ray laser fields with different laser intensities and pulse durations. The laser field is along the horizontal direction and the laser propagation is along the vertical direction.

may go to a place very far from the nucleus. Thus the dipole approximation is a good approach only for longer-wavelength, lower-intensity, and short-pulse laser fields. The laser-electron interaction is proportional to $\mathbf{A} \cdot \mathbf{k}$ and increases with the photoelectron momentum k. Thus in the nondipole approach the effect of the nondipole interactions is mainly on photoelectrons with large k, enhancing the ATI spectra significantly in the high-energy region. In addition, in longer-pulse laser fields the photoelectrons can achieve more energy and thus the enhancement of the ATI spectra can be more easily observed.

In Fig. 4, the PADs from the dipole approximation [10] are plotted. It is shown that the PADs consist of two lobes for the laser fields considered and are cylindrically symmetric with respect to the laser polarization direction. In lower-intensity laser fields, the left lobes are almost the same as the right lobes, the PADs apparently do not change with pulse duration, and the interfaces between the two lobes are very small, as shown in Figs. 4(a), 4(d), and 4(g). In contrast, in higher-intensity laser fields, the PADs change significantly with the pulse duration and the interfaces between the two lobes become large. For shorter-pulse laser fields, the laser fields along the polarization direction are quite different from those against the polarization direction, and thus the left lobes are different from the right lobes, as displayed in Figs. 4(b) and 4(c). However, for longer-pulse laser fields, the laser fields along the polarization direction are very close to those against the polarization direction and thus the left and right lobes are almost the same, as shown in Fig. 4(h) and 4(i).

In Fig. 5, the PADs obtained from the nondipole calculations are displayed. It is shown that in the lower-intensity laser fields the nondipole PADs shown in Figs. 5(a), 5(d), and 5(g) are composed of two lobes and are very close to the corresponding dipole counterparts in Figs. 4(a), 4(d), and 4(g). With increase of the laser intensity, the nondipole PADs become different from the dipole ones. In higher-intensity laser fields, with increase of the pulse duration, the distortions of the PADs become larger. In particular, two additional lobes are induced, one along and one against the laser propagation direction as shown in Figs. 5(c), 5(f), and 5(i). This is different from the results for a hydrogen atom in XUV laser fields, where only one lobe against the laser propagation direction is predicted [11,12].

To probe the mechanism of the distortion in nondipole PADs, we investigate the change in the laser-electron interaction with electron position. From Eq. (46), the dipole term is independent of $r\cos\theta$ but decreases with ω. The nondipole terms depend on $r\cos\theta$ and increase with ω except for the term with $n = 1$, which is independent of ω. The nondipole interaction for an electron far from the nucleus is larger than that for an electron close to the nucleus. Due to the dependence on $\cos\theta$ the nondipole interaction is anisotropic and largest in the directions of $\theta = 0$ and π. Thus the nondipole PADs along and against the laser propagation direction are much easier to distort than those in other directions, and the cylindrical symmetry with respect to the laser polarization direction in the dipole PADs is destroyed in the nondipole PADs.

VI. SUMMARY AND CONCLUSION

In summary, we have proposed an accurate and efficient nondipole computational approach in $\mathcal{P}$ space for the study

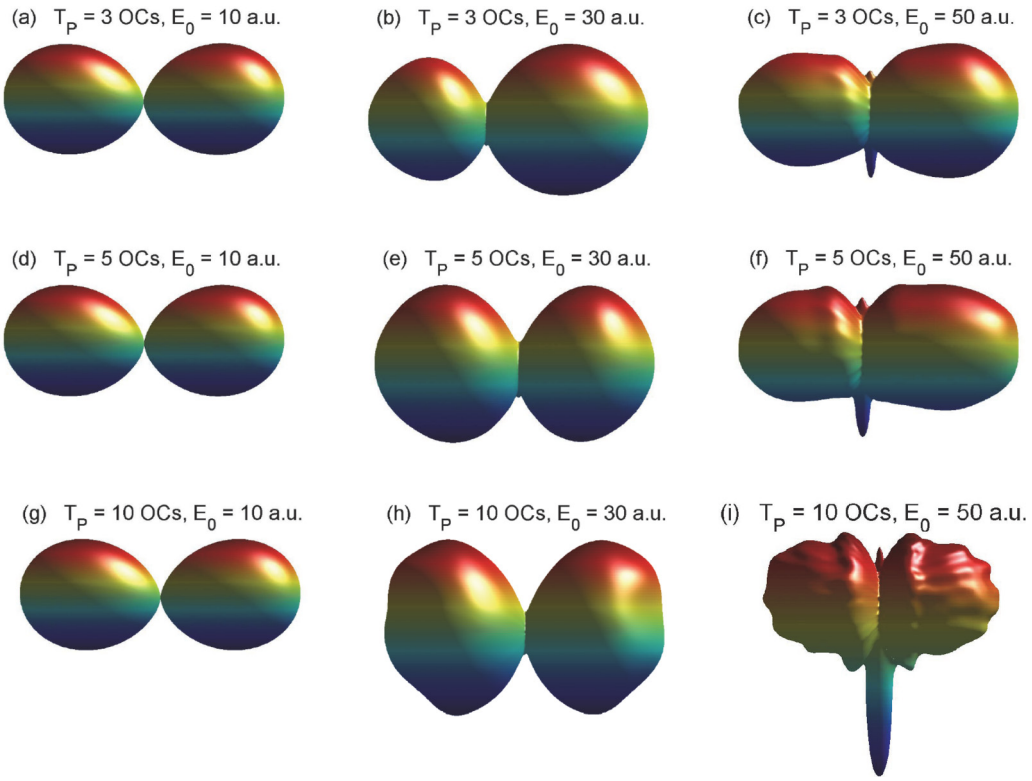

FIG. 5. (Color online) As Fig. 4 but for nondipole PADs.

of multiphoton ATI of atoms in the presence of superintense ultrashort-wavelength laser fields. This approach has been applied to the calculation of ATI spectra and PADs of a hydrogen atom exposed to superintense x-ray laser fields. It is shown that the nondipole ATI spectra and PADs are very close to the dipole ones in lower-intensity and shorter-pulse laser fields. With increase of the laser intensity and/or laser pulse duration, the nondipole results become different from the dipole ones. In higher-intensity and/or longer-pulse laser fields, the nondipole ATI peaks become less well resolved and the ATI spectra are enhanced substantially in the high-energy region. The nondipole PADs are significantly distorted along and against the laser propagation direction and the cylindrical symmetry with respect to the laser polarization direction in the dipole PADs is destroyed in the nondipole PADs. To explore the mechanisms of the substantial enhancement of the ATI spectra and the significant distortion of the PADs, we have investigated the laser-electron interaction analytically, particularly the change in the nondipole laser-electron interaction terms with the momentum and direction of the photoelectrons. We find that the nondipole laser-electron interaction terms are anisotropic and increase with the photoelectron momentum. The enhancement of the multiphoton ATI spectra in the high-energy region can be attributed directly to the fact that the nondipole laser-electron interactions increase with the photoelectron momentum, while the distortions of the PADs along and against the laser propagation directions can be attributed to the fact that the nondipole laser-electron interactions are anisotropic. Thus for a nonperturbative study of multiphoton ionization processes in superintense longer-pulse ultrashort-wavelength laser fields the dipole approximation is no longer a good approach and instead the nondipole approach should be used. Since the nondipole interactions depend on the positions of the electrons, the validity of the dipole approximation is decided not only by the laser wavelength (frequency) but also by the laser intensity and duration.

It is desirable to compare the $\mathcal{P}$-space nondipole approach proposed in this paper with other approaches. The distinctions between the $\mathcal{P}$-space nondipole approach and the $\mathcal{P}$-space dipole approximation developed in Ref. [10] are summarized below. (1) The theoretical frameworks are different. The $\mathcal{P}$-space nondipole computational approach is based on the nondipole approach, while the $\mathcal{P}$-space dipole approach is based on the dipole approximation. (2) The $\mathcal{P}$-space dipole approximation can be applied only to longer-wavelength, lower-intensity, and shorter-pulse laser fields, while the $\mathcal{P}$-space nondipole approach can, in principle, be applied to higher-intensity and/or shorter-wavelength (e.g., x-ray) as well as longer-pulse laser fields. (3) The numerical methods are different. In the $\mathcal{P}$-space dipole approximation, the calculations are two dimensional and the split-operator method is used to propagate the wave function. In the $\mathcal{P}$-space nondipole approach, due to the spatial dependence of the nondipole components of the laser fields, the calculations are three dimensional even for the hydrogen atom, making the computation quite difficult. To conquer this difficulty, a symplectic algorithm is extended to discretize the $\mathcal{P}$-space TDSE. Since the coefficient matrix in the TD matrix equation is sparse, parallel high-performance and memory-efficient software packages for sparse matrices can be used to propagate

the wave function. (4) The results from the two approaches are different. It is very clearly shown in Figs. 3–5 that both the ATI spectra and PADs of the $\mathcal{P}$-space nondipole calculations are quite different from those of the $\mathcal{P}$-space dipole calculations in higher-intensity and/or longer-pulse laser fields.

The differences between the $\mathcal{P}$-space nondipole approach and the $\mathcal{R}$-space nondipole approach recently presented in Refs. [11,12] are outlined below. (1) The $\mathcal{R}$-space nondipole approach is developed in the Kramers-Henneberger frame. In this approach, some higher-order nondipole interaction terms are neglected. The $\mathcal{P}$-space nondipole approach is proposed in $\mathcal{P}$ space. In this approach, all the nondipole interaction terms are taken into account. (2) In the $\mathcal{R}$-space nondipole approach the electron wave function is calculated by solving the TDSE in $\mathcal{R}$ space, while in the $\mathcal{P}$-space nondipole approach the electron wave function is computed by solving the TDSE in $\mathcal{P}$ space. Compared to the $\mathcal{R}$-space nondipole approach, the $\mathcal{P}$-space nondipole approach has four advantages. (1) It is more accurate. The $\mathcal{P}$-space approach is based on the fact that the momentum of an electron in any physical process is always finite and less than a certain maximum value. Thus the wave function can be more accurately calculated with a simple zero-boundary condition within a finite $\mathcal{P}$ space without any reflection on the boundary. (2) It is more efficient. After discretization using the symplectic algorithm the Hamiltonian matrix in the $\mathcal{P}$-space approach is sparse. Thus the wave function can be more efficiently propagated using parallel high-performance and memory-efficient software packages. (3) The $\mathcal{P}$-space approach includes all the nondipole interaction terms and thus can be applied to the study of atoms in superintense and ultrashort-wavelength (x-ray) laser fields where the higher-order nondipole interaction terms become more significant. (4) More elaborate structures can be obtained when the $\mathcal{P}$-space approach is applied to the study of multiphoton ATI spectra and PADs of a hydrogen atom exposed to superintense x-ray laser fields. In higher-intensity and/or longer-pulse laser fields, the multiphoton ATI spectra from the $\mathcal{P}$-space nondipole approach are enhanced substantially in the high-energy regime compared to those from the $\mathcal{P}$-space dipole approximation. The PADs from the $\mathcal{P}$-space nondipole approach are distorted significantly in higher-intensity and/or longer-pulse laser fields. In particular, two additional lobes are induced, one along and one against the laser propagation direction, which is quite different from the PADs of the $\mathcal{R}$-space nondipole approach, where only one lobe against the laser propagation direction is predicted [11,12].

ACKNOWLEDGMENTS

This work was partially supported by the U.S. Department of Energy. We would like also to acknowledge the partial support of the National Science Council of Taiwan and National Taiwan University (Grants No. 102R104021 and No. 102R8700-2).

APPENDIX A: $\mathcal{P}$-SPACE LASER-ELECTRON INTERACTIONS

Substituting Eq. (2) into Eqs. (9) and (10), we obtain

$$D(\mathbf{k},\mathbf{k}',t) = \frac{iE_0}{16\omega}\mathbf{e}_x\cdot(\mathbf{k}+\mathbf{k}')[-2e^{i\beta}\delta(\mathbf{k}'-\mathbf{k}-\mathbf{k}_L)+2e^{-i\beta}\delta(\mathbf{k}'-\mathbf{k}+\mathbf{k}_L)+e^{i\beta_3}\delta(\mathbf{k}'-\mathbf{k}-\mathbf{k}_{L3}) - e^{-i\beta_3}\delta(\mathbf{k}'-\mathbf{k}+\mathbf{k}_{L3})+e^{i\beta_4}\delta(\mathbf{k}'-\mathbf{k}-\mathbf{k}_{L4})-e^{-i\beta_4}\delta(\mathbf{k}'-\mathbf{k}+\mathbf{k}_{L4})] \tag{A1}$$

and

$$\begin{aligned} B(\mathbf{k},\mathbf{k}',t) = -\frac{E_0^2}{128\omega^2}[&8e^{i2\beta_0}\delta(\mathbf{k}'-\mathbf{k}-2\mathbf{k}_{L0})+8e^{-i2\beta_0}\delta(\mathbf{k}'-\mathbf{k}+2\mathbf{k}_{L0}).-2e^{i4\beta_0}\delta(\mathbf{k}'-\mathbf{k}-4\mathbf{k}_{L0})-2e^{-i4\beta_0}\delta(\mathbf{k}'-\mathbf{k}+4\mathbf{k}_{L0})\\ &+6e^{i2\beta}\delta(\mathbf{k}'-\mathbf{k}-2\mathbf{k}_L)+6e^{-i2\beta}\delta(\mathbf{k}'-\mathbf{k}+2\mathbf{k}_L)-4e^{i2\beta_1}\delta(\mathbf{k}'-\mathbf{k}-2\mathbf{k}_{L1})-4e^{-i2\beta_1}\delta(\mathbf{k}'-\mathbf{k}+2\mathbf{k}_{L1})\\ &-4e^{i2\beta_2}\delta(\mathbf{k}'-\mathbf{k}-2\mathbf{k}_{L2})-4e^{-i2\beta_2}\delta(\mathbf{k}'-\mathbf{k}+2\mathbf{k}_{L2})+e^{i2\beta_3}\delta(\mathbf{k}'-\mathbf{k}-2\mathbf{k}_{L3})+e^{-i2\beta_3}\delta(\mathbf{k}'-\mathbf{k}+2\mathbf{k}_{L3})\\ &+e^{i2\beta_4}\delta(\mathbf{k}'-\mathbf{k}-2\mathbf{k}_{L4})+e^{-i2\beta_4}\delta(\mathbf{k}'-\mathbf{k}+2\mathbf{k}_{L4})-12\delta(\mathbf{k}'-\mathbf{k})], \end{aligned} \tag{A2}$$

where $a_0 = \pi/\omega T_P$, $\mathbf{k}_{L0} = a_0\mathbf{k}_L$, $\mathbf{k}_{L1} = (1+a_0)\,\mathbf{k}_L$, $\mathbf{k}_{L2} = (1-a_0)\mathbf{k}_L$, $\mathbf{k}_{L3} = (1+2a_0)\mathbf{k}_L$, $\mathbf{k}_{L4} = (1-2a_0)\,\mathbf{k}_L$, $\beta\,(t) = \omega t + \phi$, $\beta_0(t) = a_0\omega t$, $\beta_1(t) = (1+a_0)\omega t + \phi$, $\beta_2\,(t) = (1-a_0)\omega t + \phi$, $\beta_3\,(t) = (1+2a_0)\omega t + \phi$, and $\beta_4\,(t) = (1-2a_0)\omega t + \phi$. It is easy to verify that $D^\dagger(\mathbf{k}',\mathbf{k},t) = D(\mathbf{k},\mathbf{k}',t)$ and $B^\dagger(\mathbf{k}',\mathbf{k},t) = B(\mathbf{k},\mathbf{k}',t)$. Thus the $\mathcal{P}$-space Hamiltonian given by Eq. (7), $H(\mathbf{k},\mathbf{k}',t)$, is Hermitian.

APPENDIX B: $\mathcal{P}$-SPACE PARTIAL-WAVE LASER-ELECTRON INTERACTIONS

Substituting Eqs. (A1) and (A2) into Eqs. (17) and (18), respectively, we obtain

$$\begin{aligned} D_{lm,l'm'}(k,k',t) = -\frac{E_0 i}{16\omega}\{&2[e^{i\beta}\lambda_{lm,l'm'}(k,k',k_L)-e^{-i\beta}\lambda^\dagger_{lm,l'm'}(k,k',k_L)]-[e^{i\beta_3}\lambda_{lm,l'm'}(k,k',k_{L3})-e^{-i\beta_3}\lambda^\dagger_{lm,l'm'}(k,k',k_{L3})]\\ &-[e^{i\beta_4}\lambda_{lm,l'm'}(k,k',k_{L4})-e^{-i\beta_4}\lambda^\dagger_{lm,l'm'}(k,k',k_{L4})]\} \end{aligned} \tag{B1}$$

and

$$
\begin{aligned}
&B_{lm,l'm'}(k,k',t)\\
&= -\frac{E_0^2}{128\omega^2}\Big\{8[e^{i2\beta_0}\eta_{lm,l'm'}(k,k',2k_{L0}) + e^{-i2\beta_0}\eta^{\dagger}_{lm,l'm'}(k,k',2k_{L0})] - 2[e^{i4\beta_0}\eta_{lm,l'm'}(k,k',4k_{L0}) + e^{-i4\beta_0}\eta^{\dagger}_{lm,l'm'}(k,k',4k_{L0})]\\
&\quad + 6[e^{i2\beta}\eta_{lm,l'm'}(k,k',2k_L) + e^{-i2\beta}\eta^{\dagger}_{lm,l'm'}(k,k',2k_L)] - 4[e^{i2\beta_1}\eta_{lm,l'm'}(k,k',2k_{L1}) + e^{-i2\beta_1}\eta^{\dagger}_{lm,l'm'}(k,k',2k_{L1})]\\
&\quad - 4[e^{i2\beta_2}\eta_{lm,l'm'}(k,k',2k_{L2}) + e^{-i2\beta_2}\eta^{\dagger}_{lm,l'm'}(k,k',2k_{L2})] + [e^{i2\beta_3}\eta_{lm,l'm'}(k,k',2k_{L3}) + e^{-i2\beta_3}\eta^{\dagger}_{lm,l'm'}(k,k',2k_{L3})]\\
&\quad + [e^{i2\beta_4}\eta_{lm,l'm'}(k,k',2k_{L4}) + e^{-i2\beta_4}\eta^{\dagger}_{lm,l'm'}(k,k',2k_{L4})] - 12\frac{k}{k'}\delta(k'-k)\delta_{ll'}\delta_{mm'}\Big\},
\end{aligned}
\tag{B2}
$$

where

$$
\begin{aligned}
\lambda_{lm,l'm'}(k,k',K) &= kk'\int\!\!\int Y^*_{lm}(\theta,\phi)(k_x+k'_x)\delta(\mathbf{k}'-\mathbf{k}-\mathbf{K})Y_{l'm'}(\theta',\phi')d\Omega\, d\Omega'\\
&= \frac{1}{4}k\sqrt{\frac{(2l+1)}{(2l'+1)}\frac{\Gamma(l-m+1)}{\Gamma(l+m+1)}\frac{\Gamma(l'-m'+1)}{\Gamma(l'+m'+1)}}\Bigg(\delta_{mm'+1}\Big\{\zeta_{lm,l'-1m'+1}(k,k',K) - \zeta_{lm,l'+1m'+1}(k,k',K)\\
&\quad + \frac{(2l'+1)}{(2l+1)}\frac{k}{k'}[(l-m+2)(l-m+1)\zeta_{l+1m-1,l'm'}(k,k',K) - (l+m)(l+m-1)\zeta_{l-1m-1,l'm'}(k,k',K)]\Big\}\\
&\quad + \delta_{mm'-1}\Bigg[\frac{(2l'+1)}{(2l+1)}\frac{k}{k'}[\zeta_{l-1m+1,l'm'}(k,k',K) - \zeta_{l+1m+1,l'm'}(k,k',K)]\\
&\quad + (l'-m'+2)(l'-m'+1)\zeta_{lm,l'+1m'-1}(k,k',K) - (l'+m')(l'+m'-1)\zeta_{lm,l'-1m'-1}(k,k',K)\Bigg]\Bigg),
\end{aligned}
\tag{B3}
$$

$$
\begin{aligned}
\eta_{lm,l'm'}(k,k',K) &= kk'\int\!\!\int Y^*_{lm}(\theta,\phi)\delta(\mathbf{k}'-\mathbf{k}-\mathbf{K})Y_{l'm'}(\theta',\phi')d\Omega d\Omega'\\
&= \frac{1}{2}\frac{k}{k'}\sqrt{(2l+1)(2l'+1)\frac{\Gamma(l-m+1)}{\Gamma(l+m+1)}\frac{\Gamma(l'-m'+1)}{\Gamma(l'+m'+1)}}\zeta_{lm,l'm'}(k,k',K)\,\delta_{mm'},
\end{aligned}
\tag{B4}
$$

and

$$
\zeta_{lm,l'm'}(k,k',K) = \int P_l^m(\cos\theta)\delta(k'-q)P_{l'}^{m'}(\cos\theta_q)d\cos\theta. \tag{B5}
$$

Here, $\eta^{\dagger}_{lm,l'm'}(k,k',K)$ and $\lambda^{\dagger}_{lm,l'm'}(k,k',K)$ are the conjugate transposes of $\eta_{lm,l'm'}(k,k',K)$ and $\lambda_{lm,l'm'}(k,k',K)$, respectively, and $P_l^m(\cos\theta)$ is the associated Legendre function. If $\mathbf{K}$ is a vector along the z axis and $\mathbf{k}$ is a vector arbitrarily oriented, the spherical coordinates (q,θ_q,ϕ_q) of a vector $\mathbf{q}=\mathbf{k}+\mathbf{K}$ are computed from

$$
q = \sqrt{k^2+2kK\cos\theta+K^2},\quad \theta_q = \tan^{-1}\left(\frac{k\sin\theta}{k\cos\theta+K}\right),\quad \phi_q=\phi, \tag{B6}
$$

where $K=|\mathbf{K}|$ and (k,θ,ϕ) are the spherical coordinates of the vector $\mathbf{k}$.

From Eqs. (B1) to (B4), $D_{lm,l'm'}(k,k',t)\neq 0$ when and only when $m'=m\pm 1$ and $B_{lm,l'm'}(k,k',t)\neq 0$ when and only when $m'=m$. Thus $D(t)=\{D_{lm,l'm'}(k,k',t)\}$ and $B(t)=\{B_{lm,l'm'}(k,k',t)\}$ are sparse matrices. It is easy to verify that when $\mathbf{k}_L=\mathbf{0}$ the nondipole approach is degraded to the dipole approximation [10].

[1] J. Feldhaus, J. Arthur, and J. B. Hastings, J. Phys. B **38**, S799 (2005).

[2] W. Ackermann *et al.*, Nat. Photon. **1**, 336 (2007).

[3] C. Gutt *et al.*, Phys. Rev. B **79**, 212406 (2009).

[4] M. Hoener *et al.*, Phys. Rev. Lett. **104**, 253002 (2010).

[5] L. Fang, M. Hoener, O. Gessner, F. Tarantelli, S. T. Pratt, O. Kornilov, C. Buth, M. Gühr, E. P. Kanter, C. Bostedt, J. D. Bozek, P. H. Bucksbaum, M. Chen, R. Coffee, J. Cryan, M. Glownia, E. Kukk, S. R. Leone, and N. Berrah, Phys. Rev. Lett. **105**, 083005 (2010).

[6] J. P. Cryan *et al.*, Phys. Rev. Lett. **105**, 083004 (2010).

[7] W. Li, R. R. Lucchese, A. Doyuran, Z. Wu, H. Loos, G. E. Hall, and A. G. Suits, Phys. Rev. Lett. **92**, 083002 (2004).

[8] N. Rohringer and R. Santra, Phys. Rev. A **76**, 033416 (2007).

[9] A. A. Sorokin, S. V. Bobashev, K. Tiedtke, and M. Richter, J. Phys. B **39**, L299 (2006).

[10] Z. Zhou and Shih-I Chu, Phys. Rev. A **83**, 013405 (2011).

[11] M. Førre, S. Selstø, J. P. Hansen, and L. B. Madsen, Phys. Rev. Lett. **95**, 043601 (2005).

[12] M. Førre, J. P. Hansen, L. Kocbach, S. Selstø, and L. B. Madsen, Phys. Rev. Lett. **97**, 043601 (2006).

[13] M. Førre, Phys. Rev. A **74**, 065401 (2006).

[14] M. Førre, S. Selstø, J. P. Hansen, T. K. Kjeldsen, and L. B. Madsen, Phys. Rev. A **76**, 033415 (2007).

[15] R. H. Landau, Phys. Rev. C **27**, 2191 (1983).

[16] K. M. Maung, D. E. Kahana, and J. W. Norbury, Phys. Rev. D **47**, 1182 (1993).
[17] Y. Rae Kwon and F. Tabakin, Phys. Rev. C **18**, 932 (1978).
[18] I. A. Ivanov and J. Mitroy, Comput. Phys. Commun. **134**, 317 (2001).
[19] X. M. Tong and S. I. Chu, Chem. Phys. **217**, 119 (1997).
[20] Z. Zhou and Shih-I Chu, Phys. Rev. A **71**, 022513 (2005).
[21] Z. Zhou, P. Ding, and S. Pan, J. Korean Phys. Soc. **32**, 417 (1998).
[22] INTEL MATH KERNEL LIBRARY, http://software.intel.com/en-us/intel-mkl.